

Covalent Sulfur-Oxygen linkages Enhanced Localized Acid Environment Coupled with Hydrogen Spillover Effect for Boosting Hydrogen Evolution Reaction Kinetics

Xiao Zhang^{1#}, Guimeng Peng^{1#}, Xuwen Deng¹, Yaoyao Wang¹, Sunpeng Shan¹,
Yuhong Bian¹, Zhiwei Shu¹, Jianrong Chen^{1*}, Jian Yang^{2*}, Yang Jiao^{1*}

1 College of Geography and Environmental Sciences, College of Chemistry and
Materials Science, Zhejiang Normal University, Jinhua, 321004, China.

2 Jinhua Advanced Research Institute, Jinhua 321019, China

[#]These two authors contributed equally.

*Corresponding author:

Yang Jiao, Jian Yang and Jianrong Chen; E-mail: yangjiao@zjnu.edu.cn,
yj5210210@163.com and cjr@zjnu.cn. Fax: (+86)-0579-82291275.

Electrochemical measurements

1. Preparation of electrodes

The sample (80%), carbon black (10%), and polyethylene difluoride (10%) are mixed and magnetic stirred for 12 h to obtain a black paste substance, which would be coated on dry nickel foam, and subsequently dried under vacuum at 120 °C for 10 h to obtain the working electrode. The catalyst loading on the nickel foam between 2 ~ 2.8 mg.

2. Raw materials

Iron (II) chloride tetrahydrate ($\text{FeCl}_2 \cdot 4\text{H}_2\text{O}$), copper (II) chloride dihydrate ($\text{CuCl}_2 \cdot 2\text{H}_2\text{O}$), Trimesic acid (H_3BTC), N, N-Dimethylformamide (DMF), Polyvinylidene fluoride (PVDF), 1-Methyl-2-pyrrolidinone (NMP), absolute ethanol, potassium hydroxide (KOH) are purchased by Sinopharm Chemical Reagent Co, Ltd. All chemicals are utilized as received without additional purification.

3. Electrocatalytic performance

The three-electrode setup comprises a working electrode (comprising the active material), a reference electrode (Hg/HgO), and counter electrodes for OER and HER, utilizing platinum plates and carbon rods respectively. The electrolyte utilized is 1 M KOH. Linear sweep voltammetry (LSV) curves and cycling stability assessments are conducted using the CHI 660E electrochemical workstation (Shanghai CH Instrument). A reversible hydrogen electrode (RHE) serves as the reference to calibrate all potentials. The LSV curve is adjusted utilizing the equation $E_{\text{RHE}} = E_{\text{Hg/HgO}} + 0.0591\text{pH} + 0.098$.

The potential range applied during the cycling test was from -2 V to +2 V, with a scan rate of 0.002 V s⁻¹, and the number of cycles was 1.

4. Material characterization

The synthesized products' morphological characteristics were examined using scanning electron microscopy (SEM, Gemini SEM 300) and high-resolution transmission electron microscopy (TEM, JEM-2100F, operated at 200 kV). Elemental composition analysis was carried out *via* X-ray diffraction (XRD, Bruker, D8 Advance) employing Cu K α radiation. X-ray photoelectron spectroscopy (XPS, Thermo Fisher Scientific, ESCALAB 250Xi) and Fourier transform infrared spectroscopy (FTIR, Thermo Nicolet, NEXUS 670) were employed to analyze the chemical composition of the resulting materials. Raman spectroscopy analysis was performed using a Renishaw in Via-Reflex instrument (England) with an excitation wavelength of 532 nm. Thermal gravimetric analysis (TGA) was conducted using an STA449 F5 instrument under a N₂ atmosphere with a heating rate of 5 °C min⁻¹.

5. TOF calculation

The turnover frequency (TOF) was calculated using the following formula:

$$\text{TOF} = j \times N_A / (F \times n \times G)$$

Where j , N_A , F , n , and G represent current density, the Avogadro constant, the Faraday constant, the number of electrons transferred to generate one molecule of the product, and the surface concentration or exact number of active sites catalyzing the reaction (m⁻²), respectively. The value of n is 2 for HER and 4 for OER.

6. Computational details of DFT

All computational simulations in this study were performed using spin-polarized density functional theory (DFT) within the Vienna Ab initio Simulation Package (VASP). The calculations employed the projector augmented-wave (PAW) method to

describe the ion-electron interactions, and the generalized gradient approximation (GGA) with the Perdew–Burke–Ernzerhof (PBE) functional for the exchange-correlation energy. The Kohn–Sham single-electron states were expanded in a plane-wave basis set with a cutoff energy of 500 eV. The energy and force convergence criteria for structural optimization were set to 10^{-6} eV and 0.01 eV/Å, respectively. For subsequent electronic structure calculations, a $10 \times 10 \times 1$ k-point grid centered at the Gamma (Γ) point was used. Van der Waals interactions were taken into account using Grimme's DFT-D3 method. The heterojunction model was constructed by interfacing the (311) surface of CuFe_2O_4 with the (112) surface of CuFeS_2 to form a CuFe_2O_4 - CuFeS_2 composite. The supercell dimensions were set to $15.2834 \text{ Å} \times 11.4379 \text{ Å}$, and a vacuum layer of 15 Å was added along the c-axis to eliminate spurious interactions between periodic images. To simulate realistic surface conditions and enhance interfacial coupling, an oxygen vacancy was introduced on the CuFe_2O_4 side near the interface. This oxygen-deficient site was further used to chemically anchor a sulfur atom from the CuFeS_2 layer, forming a bridging S-O bond that stabilizes the heterointerface.

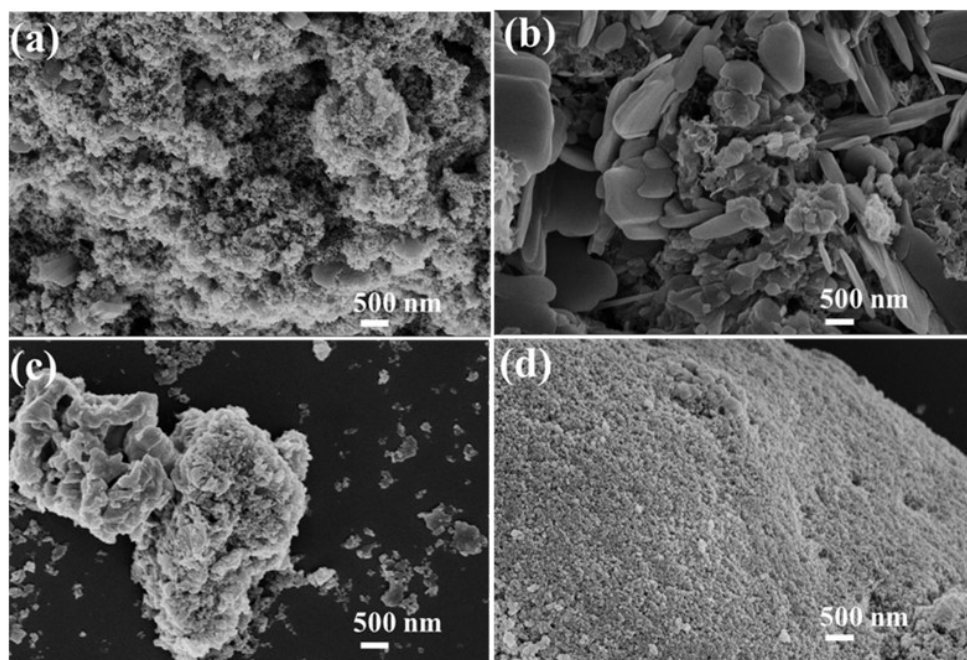


Figure S1. SEM images of (a-b) CuFe-MOF/S-0.5 and CuFe-MOF/S-2; (c-d) CuFe₂O₄@ CuFeS₂-0.5 and CuFe₂O₄@CuFeS₂-2.

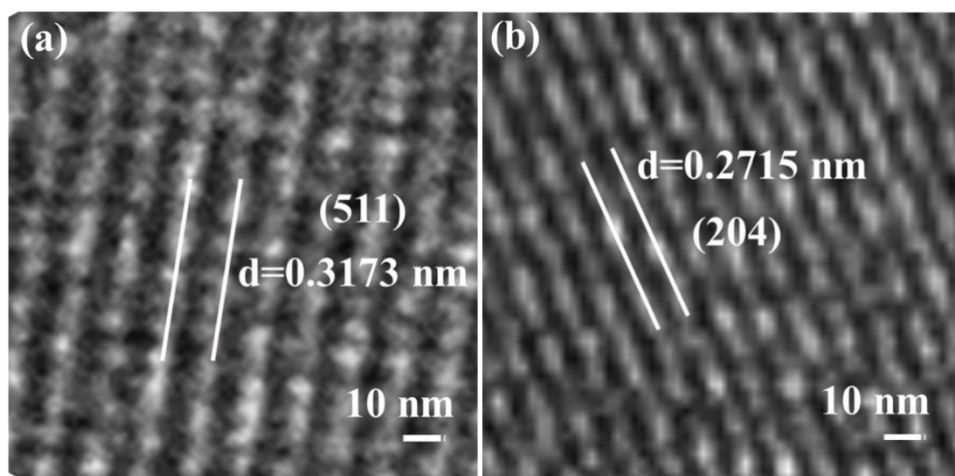


Figure S2. The enlarged HRTEM images of the lattice fringes of (a) CuFe₂O₄ and CuFeS₂.

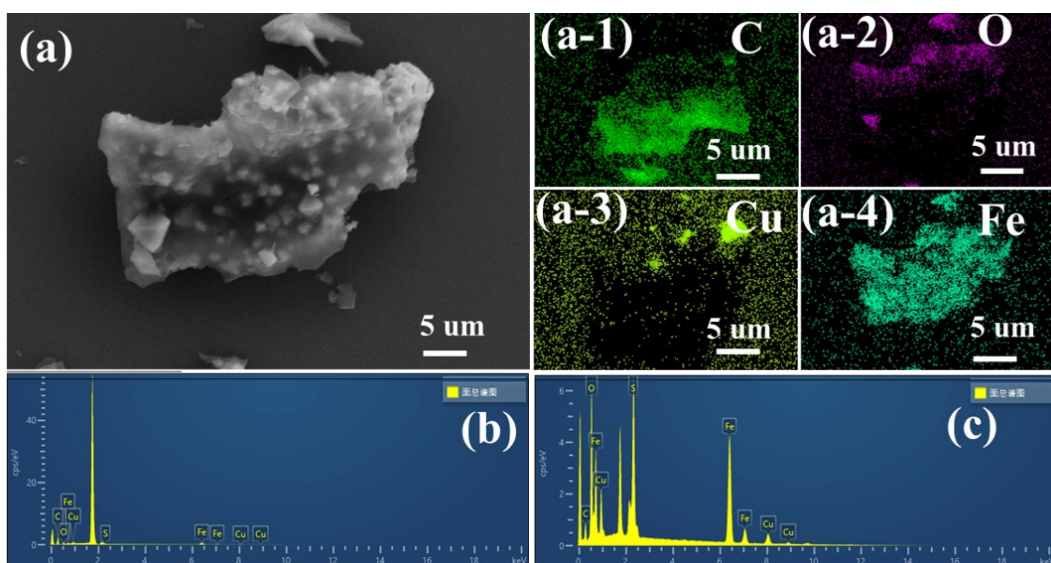


Figure S3. (a) SEM image and elemental mapping of CuFe₂O₄@Cu; EDX spectrum of (b) CuFe₂O₄@Cu and (c) CuFe₂O₄@CuFeS₂-1.

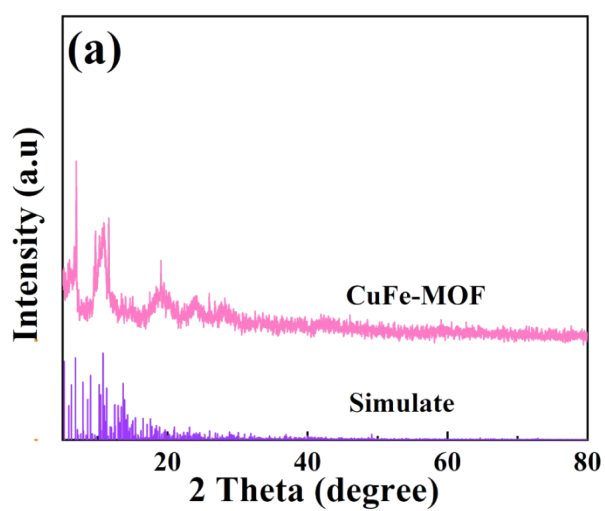


Figure S4. (a) XRD pattern of CuFe-MoF.

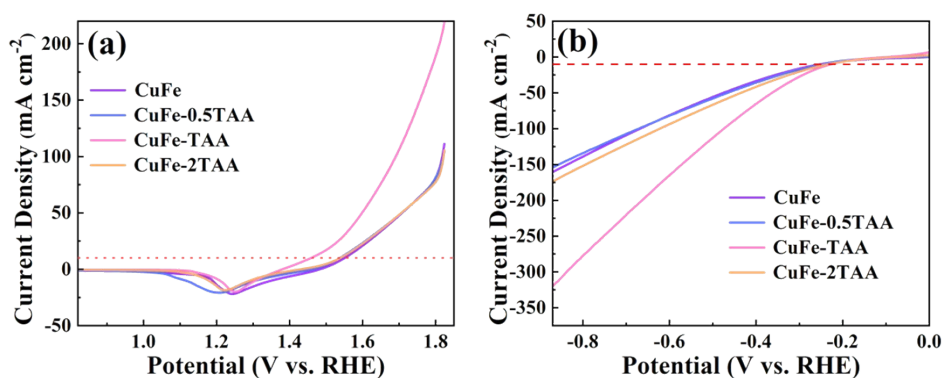


Figure S5. (a) LSV curves for OER of different samples; (b) LSV curves for HER of different samples.

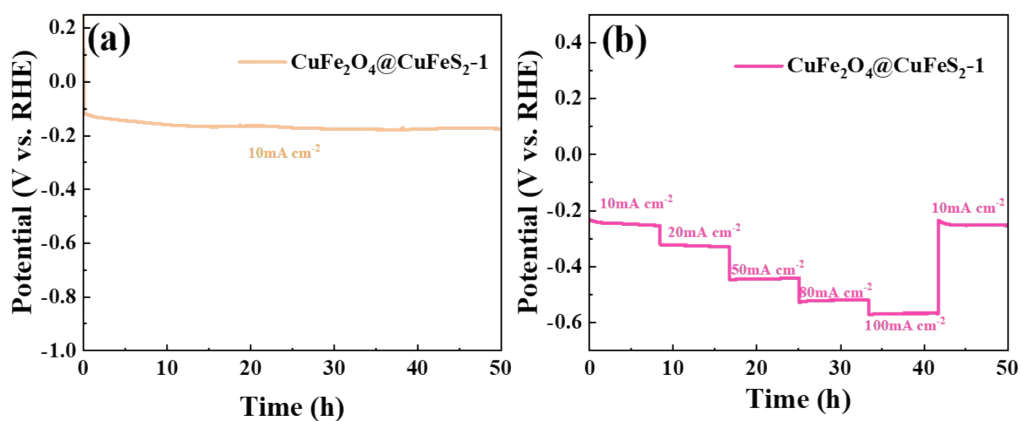


Figure S6. (a) Cycling stability at 10 mA cm⁻²; (b) Current densities at multiple scan rates (10, 20, 50, 80 and 100 mA cm⁻²).

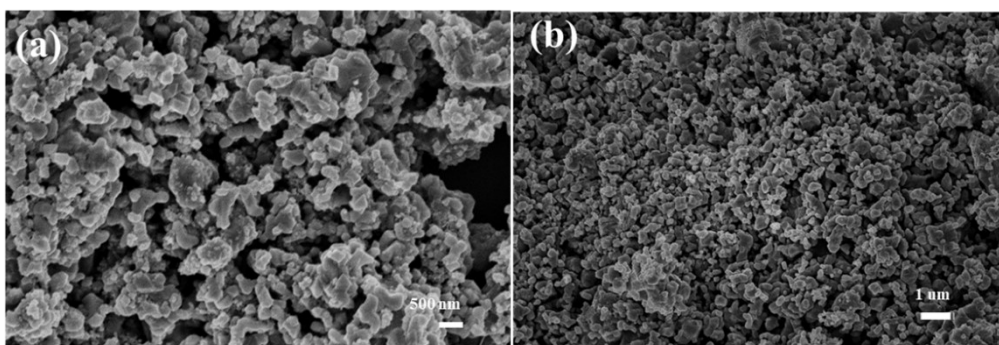


Figure S7. SEM images of CuFe₂O₄@CuFeS₂-1 after Cycling stability of 50 hour at 10 mA cm⁻².

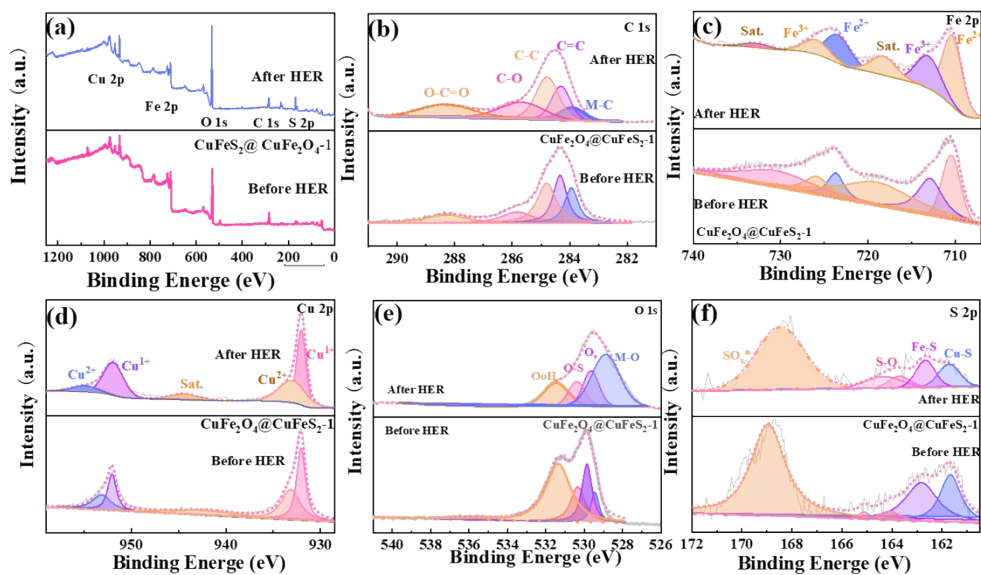


Figure S8. Resolution XPS spectrum of (a) full spectra; (b) C 1s; (c) Fe 2p; (d) Cu 3d; (e) O 1s; (f) S 2p.

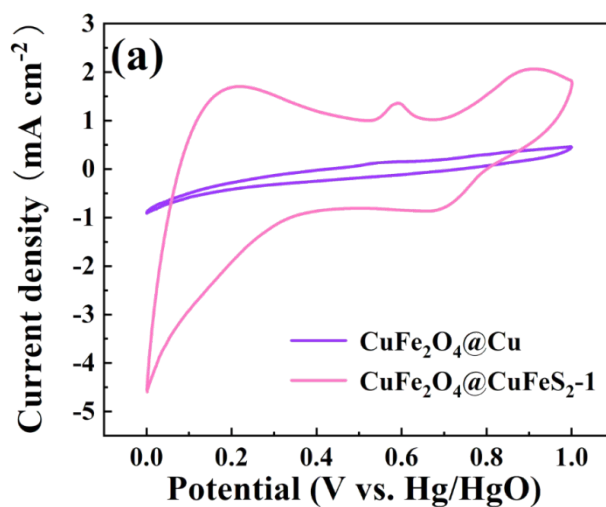


Figure S9. (a) Cyclic voltammograms at 10 mV s^{-1} in 1.0 M KOH .

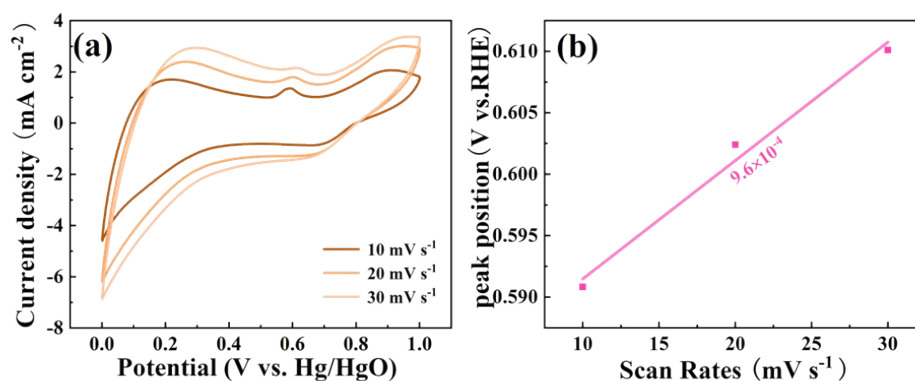


Figure S10. Cyclic voltammetry curves of (a) $\text{CuFe}_2\text{O}_4@\text{CuFeS}_2\text{-1}$; (b) The linear plots of peak potentials for $\text{CuFe}_2\text{O}_4@\text{CuFeS}_2\text{-1}$ vs. scan rates.

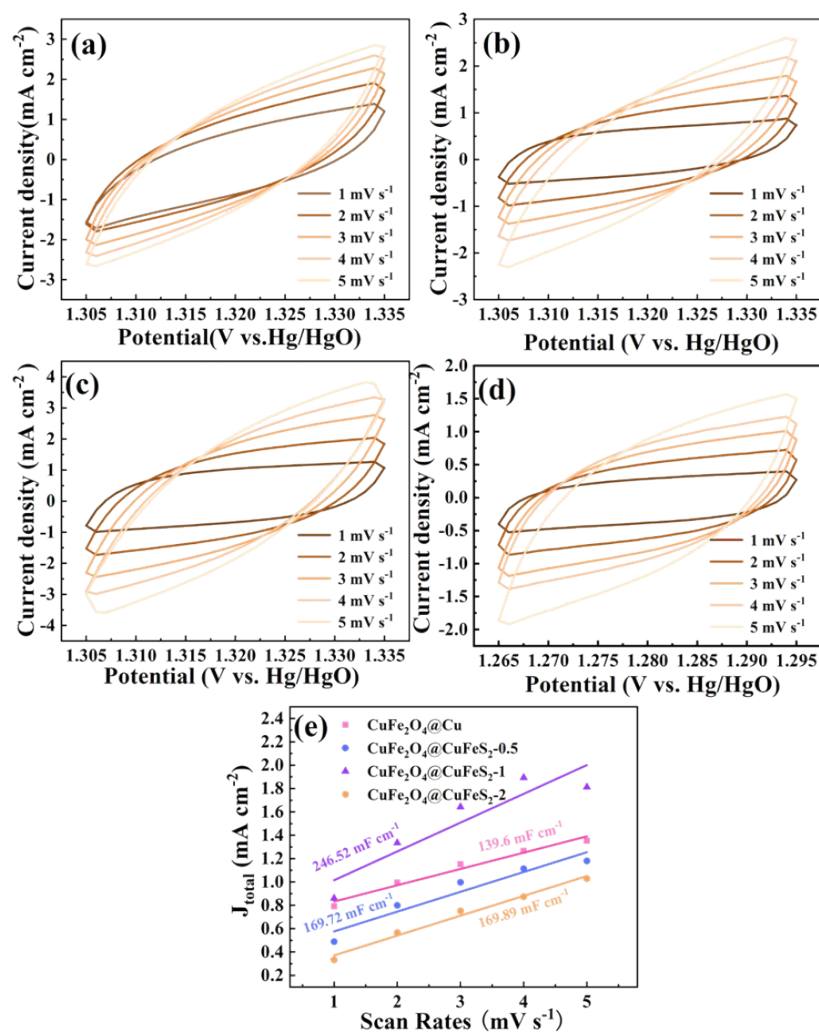


Figure S11. Cyclic voltammograms curves of (a) CuFe_2O_4 ; (b) $\text{CuFe}_2\text{O}_4@\text{Cu-0.5}$; (c) $\text{CuFe}_2\text{O}_4@\text{CuFeS}_2\text{-1}$; (d) $\text{CuFe}_2\text{O}_4@\text{CuFeS}_2\text{-2}$; (e) The electrical double-layer capacitor values for different samples.

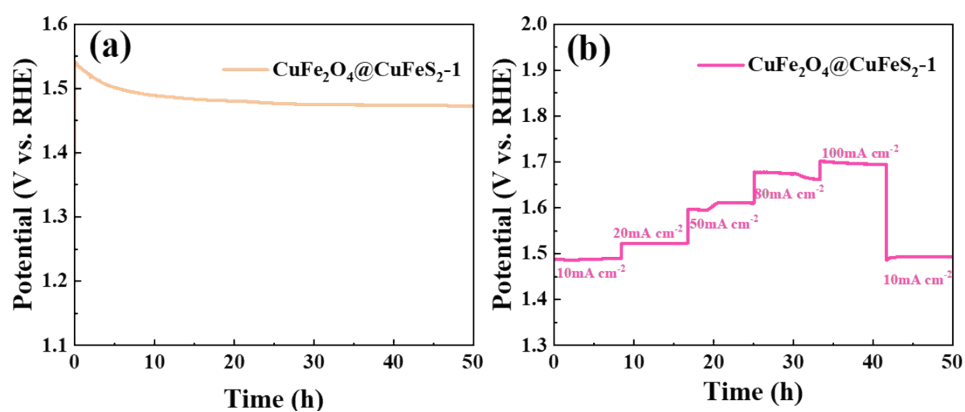


Figure S12. (a) Cycling stability at 10 mA cm^{-2} ; (b) Current densities at multiple scan rates ($10, 20, 50, 80$ and 100 mA cm^{-2}).

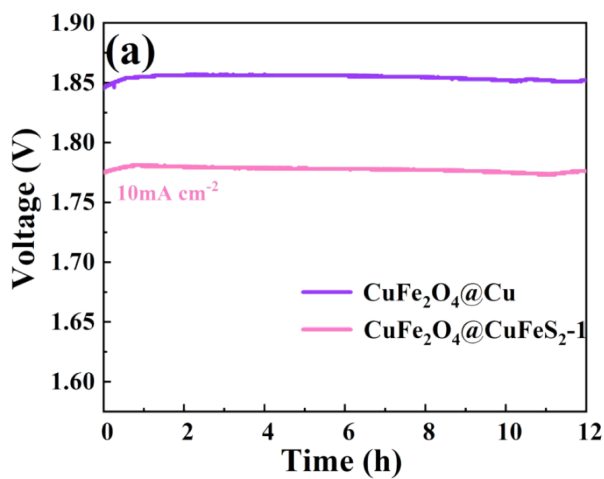


Figure S13. (a) Cycling stability curve of overall water splitting at a scan rate of 10 mA cm^{-2} .

Table S1. Atomic ratios (%) of different elements as measured by XPS.

Electrode material	C 1s	Fe 2p	Cu 2p	O 1s	S 2p
$\text{CuFe}_2\text{O}_4@\text{Cu}$	75.63	2.92	1.19	16.08	/
$\text{CuFe}_2\text{O}_4@\text{CuFeS}_2-1$	26.13	18	4.86	46.59	4.42

Table S2. Comparison of OER between the CuFe₂O₄@CuFeS₂-1 and oxide or sulfide electrode materials.

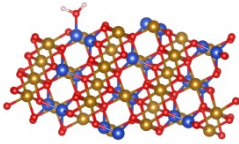
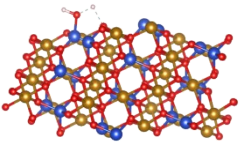
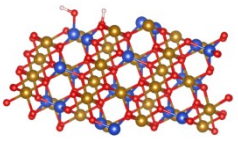
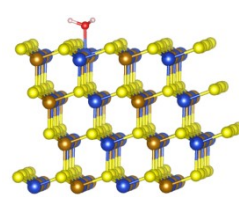
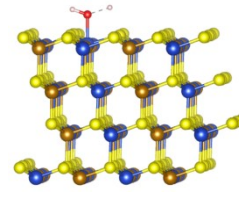
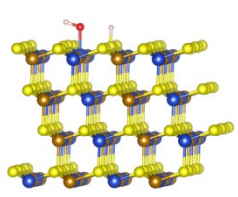
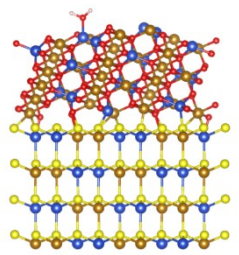
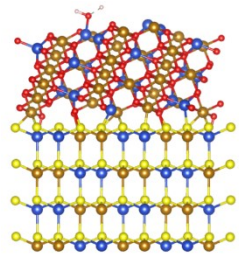
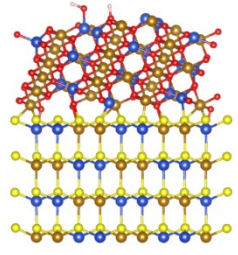
Electrode material	Electrolyte	Overpotential (mV)	References
CuFe₂O₄@CuFeS₂-1	1 M KOH	150 (10 mA cm⁻²)	This work
CuFeS ₂	1 M KOH	320 (10 mA cm ⁻²)	¹
FeS ₂	1 M KOH	330 (10 mA cm ⁻²)	¹
CuS	1 M KOH	354 (10 mA cm ⁻²)	¹
Fe-Ni ₃ S ₂ /Ni ₂ P	1 M KOH	172 (10 mA cm ⁻²)	²
NiMoO _x /NiMoS	1 M KOH	186 (10 mA cm ⁻²)	³
(Ru-Ni)O _x	1 M KOH	237 (10 mA cm ⁻²)	⁴
CuFe ₂ O ₄	1 M KOH	474 (10 mA cm ⁻²)	⁵
Fe ₃ O ₄ @Co ₉ S ₈ /rGO-2	1 M KOH	340 (10 mA cm ⁻²)	⁶
CSC-MoS ₂ @CoS ₂ -24	1 M KOH	350 (10 mA cm ⁻²)	⁷
NiFeV/NF	1 M KOH	218 (10 mA cm ⁻²)	⁸
H-Ag-NiCo-PBA@NiFe-LDH	1 M KOH	190 (10 mA cm ⁻²)	⁹
Co ₃ O ₄ /gCN	1 M KOH	286.2 (10 mA cm ⁻²)	¹⁰

Table S3. Comparison of HER between the CuFe₂O₄@CuFeS₂-1 and oxide or sulfide

electrode materials.

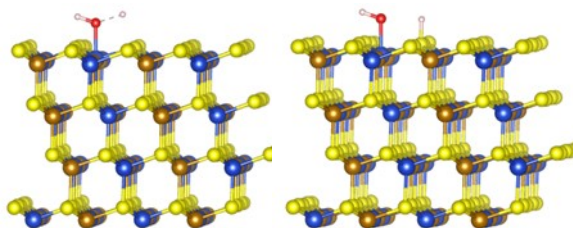
Electrode material	Electrolyte	Overpotential (mV)	References
CuFe₂O₄@CuFeS₂-1	1 M KOH	190 (10 mA cm⁻²)	This work
NiFe ₂ O ₄	1 M KOH	290 (10 mA cm ⁻²)	11
Co ₂ FeO ₄	1 M KOH	372 (10 mA cm ⁻²)	12
Co ₂ FeO ₄ @PdO	1 M KOH	269 (10 mA cm ⁻²)	12
Co ₃ S ₄ @MoS ₂	1 M KOH	280(10 mA cm ⁻²)	13
CuS	1 M KOH	255 (10 mA cm ⁻²)	1
FeS ₂	1 M KOH	279 (10 mA cm ⁻²)	1
CuFe ₂ O ₄	1 M KOH	320 (10 mA cm ⁻²)	14
CSC-MoS ₂ @CoS ₂ -24	1 M KOH	241.5 (10 mA cm ⁻²)	7
Ce _{0.3} -MoS ₂	1 M KOH	183.23 (10 mA cm ⁻²)	15
Co ₃ O ₄ /gCN	1 M KOH	294.1 (10 mA cm ⁻²)	10

Table S4. The corresponding intermediate structure for HER on different samples.

	*H₂O	*H-OH	*H+OH
CuFe₂O₄			
CuFeS₂			
CuFe₂O₄@ CuFeS₂-1			

References

1. A. Sathyaseelan, D. Kesavan, S. Manoharan, *Acs Appl Energ Mater*, 2021, **4**, 7020-7029.
2. X. Y. Wang, X. Yu, J. L. Bai, G. J. Yuan, P. Y. He, Y. Q. Zhu, S. Wu, F. Qin and L. L. Ren, *Electrochim. Acta*, 2023, **458**, 142524.
3. P. L. Zhai, Y. X. Zhang, Y. Z. Wu, J. F. Gao, B. Zhang, S. Y. Cao, Y. T. Zhang, Z. W. Li, L. C. Sun and J. G. Hou, *Nat. Commun.*, 2020, **11**, 5462.
4. H. Zhang, Y. Lv, C. Chen, C. Lv, X. Wu, J. Guo and D. J. A. C. B. E. Jia, *Appl. Catal., B*, 2021, **298**, 120611.
5. M. Li, M. Lu, J. Yang, J. Xiao, L. Han, Y. Zhang and X. Bo, *J. Alloys Compd.*, 2019, **809**, 151766.
6. J. Yang, G. Zhu, Y. Liu, J. Xia, Z. Ji, X. Shen and S. J. A. F. M. Wu, *Adv. Funct. Mater.*, 2016, **26**,



- 4712-4721.
7. Y. Cheng, X. Zhou, Q.-M. Pan, L.-F. Zhang, Y.-F. Cao and T. J. R. M. Qian, *Rare Met.*, 2023, **42**, 3024-3033.
 8. Q. Kong, J. Wang, Z. Liu, S. Wu, X. Tong, N. Zong, B. Huang, R. Xu and L. J. D. T. Yang, *Dalton T*, 2023, **52**, 16963-16973.
 9. W. Cao, J. Wu, C. Zhou, X. Gao, E. Hu, J. Zhang and Z. J. S. Chen, *Small*, 2024, **20**, 2309769.
 10. A. Zabielaite, A. Balciunaite, D. Upskuvienne, D. Simkunaite, R. Levinas, G. Niaura, J. Vaiciuniene, V. Jasulaitiene, L. Tamasauskaite-Tamasiunaite and E. J. M. Norkus, *Materials*, 2023, **16**, 5923.
 11. N. Dalai, B. Mohanty, A. Mitra and B. Jena, *Chemistryselect*, 2019, **4**, 7791-7796.
 12. A. Hanan, M. N. Lakhani, D. Shu, A. Hussain, M. Ahmed, V. Kumar, D. X. Cao and I. A. Soomro, *Int. J. Hydrogen Energy*, 2023, **48**, 19494-19508.
 13. Y. N. Guo, J. Tang, Z. L. Wang, Y. M. Kang, Y. Bando and Y. Yamauchi, *Nano Energy*, 2018, **47**, 494-502.
 14. H. Belhadj, Y. Messaoudi, M. R. Khelladi and A. J. I. J. o. H. E. Azizi, *Int. J. Hydrogen Energy*, 2022, **47**, 20129-20137.
 15. L. Kong, C. Gao, Z. Liu, L. Pan, P. Yin and J. J. C. E. J. Lin, *Chen Eng J*, 2024, **479**, 147725.